PAPER • **OPEN ACCESS**

Animal tissue-based quantitative comparison of dual-energy CT to SPR conversion methods using high-resolution gel dosimetry

IOP Publishing Phys. Med. Biol. 66 (2021) 075009 https://doi.org/10.1088/1361-6560/abbd14

Physics in Medicine & Biology

IPEM Institute of Physics and Engineering in Medicine

OPEN ACCESS

RECEIVED
10 June 2020

REVISED
7 August 2020

ACCEPTED FOR PUBLICATION
30 September 2020

PUBLISHED
24 March 2021

PAPER

Animal tissue-based quantitative comparison of dual-energy CT to SPR conversion methods using high-resolution gel dosimetry

K B Niepel[1], M Stanislawski[1], M Wuerl[1], F Doerringer[1], M Pinto[1], O Dietrich[3], B Ertl-Wagner[3,4], A Lalonde[5,6], H Bouchard[5], E Pappas[7], I Yohannes[2], M Hillbrand[2], G Landry[8,1,9,*] and K Parodi[1,*]

[1] Department of Medical Physics, Ludwig-Maximilian Universität München (LMU Munich), Munich, Germany
[2] Rinecker Proton Therapy Center, Munich, Germany
[3] Department of Radiology, Ludwig-Maximilian University Hospital, Munich, Germany
[4] The Hospital for Sick Children, Department of Medical Imaging, University of Toronto, Toronto, Canada
[5] Département de Physique, Université de Montréal, Montreal, Canada
[6] Department of Radiation Oncology, Massachusetts General Hospital and Harvard Medical School, Boston, MA, United States of America
[7] Radiology & Radiotherapy Sector, Department of Biomedical Sciences, University of West Attica, Athens, Greece
[8] Department of Radiation Oncology, Ludwig-Maximilian University Hospital, Munich, Germany
[9] German Cancer Consortium (DKTK), Munich, Germany
[*] Senior authorship is shared equally.

E-mail: k.niepel@physik.uni-muenchen.de

Keywords: dual-energy CT, proton therapy, dosimetry, stopping power

Abstract

Dual-energy computed tomography (DECT) has been shown to allow for more accurate ion therapy treatment planning by improving the estimation of tissue stopping power ratio (SPR) relative to water, among other tissue properties. In this study, we measured and compared the accuracy of SPR values derived using both dual- and single-energy CT (SECT) based on different published conversion algorithms. For this purpose, a phantom setup containing either fresh animal soft tissue samples (beef, pork) and a water reference or tissue equivalent plastic materials was designed and irradiated in a clinical proton therapy facility. Dosimetric polymer gel was positioned downstream of the samples to obtain a three-dimensional proton range distribution with high spatial resolution. The mean proton range in gel for each tissue relative to the water sample was converted to a SPR value. Additionally, the homogeneous samples were probed with a variable water column encompassed by two ionization chambers to benchmark the SPR accuracy of the gel dosimetry. The SPR values measured with both methods were consistent with a mean deviation of 0.2%, but the gel dosimetry captured range variations up to 5 mm within individual samples.

Across all fresh tissue samples the SECT approach yielded significantly greater mean absolute deviations from the SPR deduced using gel range measurements, with an average difference of 1.2%, compared to just 0.3% for the most accurate DECT-based algorithm. These results show a significant advantage of DECT over SECT for stopping power prediction in a realistic setting, and for the first time allow to compare a large set of methods under the same conditions.

1. Introduction

The prediction of beam range in tissue is a main challenge in ion radiation therapy, with uncertainties up to 3% or more in current clinical practice (Paganetti 2012). Dual-energy computed tomography (DECT) has been shown to reduce this uncertainty in simulation studies (Yang *et al* 2010, Lalonde *et al* 2018) by improving the estimation of the stopping power ratio (SPR) in tissue relative to water, along with other tissue properties such as mass and electron density or elemental composition. This finding was later validated using tissue surrogate materials (Hunemohr *et al* 2013, 2014, Zhu and Penfold 2016, Wohlfahrt *et al* 2017). These materials were mostly homogeneous and offered the advantage of having well known material properties. However, their composition did not resemble that of human tissues well enough to utilize the information about human tissues incorporated in several newer conversion methods, such as in Yang *et al* (2010),

Saito (2012), Kanematsu *et al* (2012), Landry *et al* (2013b), Bourque *et al* (2014), Berndt (2016), Lalonde and Bouchard (2016), Mohler *et al* (2016), Saito and Sagara (2017), Lalonde *et al* (2017).

Hudobivnik *et al* (2016) calculated dose differences in a planning study using single-energy CT (SECT) and DECT images of real patients. The DECT was calculated using a combination of three proposed methods to convert DECT to relative electron density (RED) $\hat{\rho}_e$ and Z_{eff} as well as Z_{eff} to the mean ionization potential I_{tissue} using scanner specific calibration factors (Yang *et al* 2010, Saito 2012, Landry *et al* 2013b). While that study showed a significant influence of DECT-based treatment planning on dose deposition in realistic conditions, no ground truth dose distribution could be determined. Another planning study by Wohlfahrt *et al* (2017) affirmed this finding by recalculating clinical proton treatment fields for 50 patients.

Other recent studies sought to validate DECT-based conversion algorithms in animal tissues. Hunemohr *et al* (2013) compared their DECT conversion method against a SECT-based Hounsfield look-up table (HLUT) by probing the water equivalent thicknesses (WETs) along several paths in a highly inhomogeneous frozen pig head using carbon ions. Works by Taasti *et al* (2016, 2017) and Mohler *et al* (2018) aimed to create homogeneous samples from soft and bony animal tissues. They probed these samples with proton and carbon ion beams, respectively, and then compared the measured SPR values to calculations based on both a DECT algorithm and a SECT HLUT. Possible inhomogeneities were accounted for by shifting the samples between repeated proton beam probes to assess homogeneity or by using multiple samples of the same tissue type. In all three of these studies, the samples were probed either by using a variable water column encompassed by two ionization chambers or a multi-leaf ionization chamber (MLIC) with range shifters, resulting in one dimensional, laterally integrated depth dose curves. These curves have a high longitudinal resolution, but are sensitive to lateral alignment and fail to capture the unavoidable inhomogeneities of *ex-vivo* animal samples.

A study by Bär *et al* (2017) again looked at a setup with heterogeneous animal samples, using the dose extinction method over an ion chamber detector array to obtain a three-dimensional dose distribution and compared it to Monte Carlo simulations based on two of their DECT algorithms Bourque *et al* (2014) and Lalonde *et al* (2017) and a stoichiometric SECT calibration. However, the lateral resolution was limited by a 7.62 mm distance between the centers of the ionization chambers, and the signal of each detector was still laterally integrated over the chamber volume. Xie *et al* (2018) also investigated the conversion algorithm by Bourque *et al*, using two different methods. Firstly, they took one-dimensional proton transmission measurements of frozen near-homogeneous tissue samples with a MLIC. Secondly, they used Gafchromic EBT2 films to investigate the exit dose profiles of two heterogeneous phantoms comprised of combinations of soft and bony animal tissues along with homogeneous tissue surrogates and animal tissue samples as well as water. This approach yielded a two-dimensional slice of the exit dose distribution that could be compared to the dose prediction of a treatment planning system (TPS), but at the same time was very sensitive to alignment errors. Various other promising DECT-to-SPR conversion algorithms have been proposed (Landry *et al* 2011, Kanematsu *et al* 2012, Berndt 2016, Saito and Sagara 2017) but so far were not validated in animal tissue studies.

Another promising tomographic modality to extract SPR images is proton CT (Cormack 1963, Takada *et al* 1988, Penfold *et al* 2009, Rit *et al* 2013), which has been shown to perform as well as DECT conversion in terms of accuracy for tissue equivalent materials (TEMs) (Dedes *et al* 2019). Unlike DECT, such scanners are however not yet available for clinical use.

While DECT-based treatment planning is entering clinical practice (Wohlfahrt *et al* 2017), no comparison study has been published that quantifies the accuracy of the different conversion methods in experimental setups that are both realistic and allow to contrast their accuracy under similar conditions. Our study aims at filling this gap by comparing the performance of various published methods on the same dataset of fresh animal tissue samples against both one-dimensional range measurements, using a highly accurate variable water column encompassed by two parallel plate ionization chambers, and three-dimensional range maps, using a dosimetric gel with high spatial resolution (Hillbrand *et al* 2019).

2. Materials and methods

In summary, for this study, we designed PMMA phantom shells, which can house a cubic flask of dosimetric N-vinylpyrrolidone based polymer gel (VIP gel) (Pappas *et al* 1999, 2001) as well as either fresh animal tissue samples or tissue equivalent plastic samples (see figure 1). The assembled gel phantoms were irradiated in a clinical proton facility and then scanned at two different CT scanners, using both single- and dual-energy protocols. The gel flasks were then scanned in a magnetic resonance imaging (MRI) scanner to read out the gel signal. Additionally, the samples where probed with one-dimensional proton transmission measurements using an adjustable water column (PTW peakfinder, PTW, Freiburg, Germany). The peakfinder (PKF) measurements served as one-dimensional benchmark for the VIP gel.

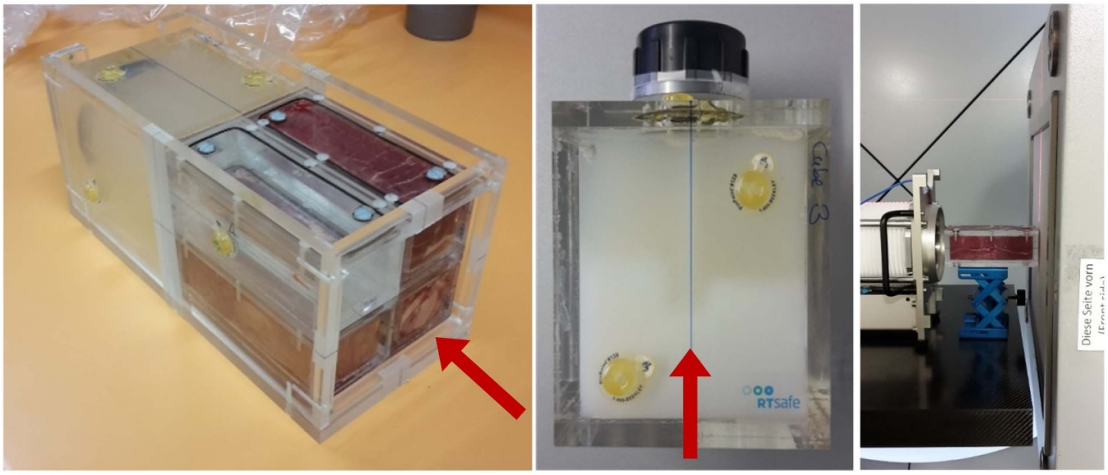

Figure 1. Fully assembled phantom with soft tissue samples and gel flask (left), irradiated gel flask (middle) and individual tissue box with PKF (right). The arrows indicate the beam direction. Reproduced with permission from RT Safe (middle figure).

Table 1. Overview of all phantom assemblies used in this study. Flasks containing dosimetric gel were housed in PMMA shells.

	Geometry	Material
Gel phantom 1	Shell 1, flask 1	3 soft tissue samples + 1 water sample
Gel phantom 2	Shell 2, flask 2	3 soft tissue samples + 1 water sample
Gel phantom 3	Shell 1, flask 3	2×4 tissue equivalent inserts (CIRS)
Calibration phantom	PMMA cylinder	9 tissue equivalent inserts (RMI)
Evaluation phantom	PMMA cylinder	8 tissue equivalent inserts (CIRS)

Table 2. Animal tissue samples used in gel phantoms and their corresponding labels.

	shell 1				shell 2			
Label	A	B	C	D	E	F	G	H
Sample	Water	Shoulder (beef)	Brain (pork)	Tongue (beef)	Water	Liver (beef)	Filet (pork)	Fat (beef)

The range distribution in gel was converted to a ground truth set of SPR values by looking at the mean ranges behind the samples relative to that of water. Two-dimensional range maps were also used to assess the homogeneity of the tissue samples, and thereby the suitability of using one-dimensional laterally integrating detectors like PKF or MLICs.

2.1. Phantom descriptions

A total of five phantom configurations where used within this study (see tables 1 and 2): three gel phantoms housing two different sets of soft tissue samples and one set of TEMs, a calibration phantom containing tissue equivalent inserts used to calibrate the CT-to-SPR conversion and an evaluation phantom containing different tissue equivalent inserts to check for potential biases in this conversion.

2.1.1. Gel phantoms

The gel phantoms used in this study consisted of a cuboid flask containing VIP gel (see section 2.2.2), reusable sample boxes that can be filled with both liquid and solid samples and an outer shell holding the gel flask and up to four sample boxes in place during irradiation and subsequent scanning. The holder has a window cut in front of the tissue boxes to minimize the amount of material in the beam path. Both the holders and the gel flasks were marked with multi-modality fiducial markers (PinPoint, Beekley Medical, Bristol, CT, United States) to allow for later image registration of the MRI and CT scans.

In this study, two soft tissue phantoms were used, each consisting of three tissue sample boxes and one sample box filled with purified water to serve as reference. The tissue samples were collected fresh from a butcher a few hours before the experiments. Table 2 gives an overview of all soft tissue samples used, with samples A–D and E–H being stacked in front of the same gel flask, respectively. Each sample was fitted into a PMMA sample box with interior dimension of 4 × 4 × 13.4 cm, packing each box as tightly as possible to avoid air pockets. The boxes were then sealed with a rubber gasket and screwed shut with plastic screws. Purified water was injected through holes in the lid of each box to supplant any residual air bubbles in the samples before these were sealed as well with additional plastic screws.

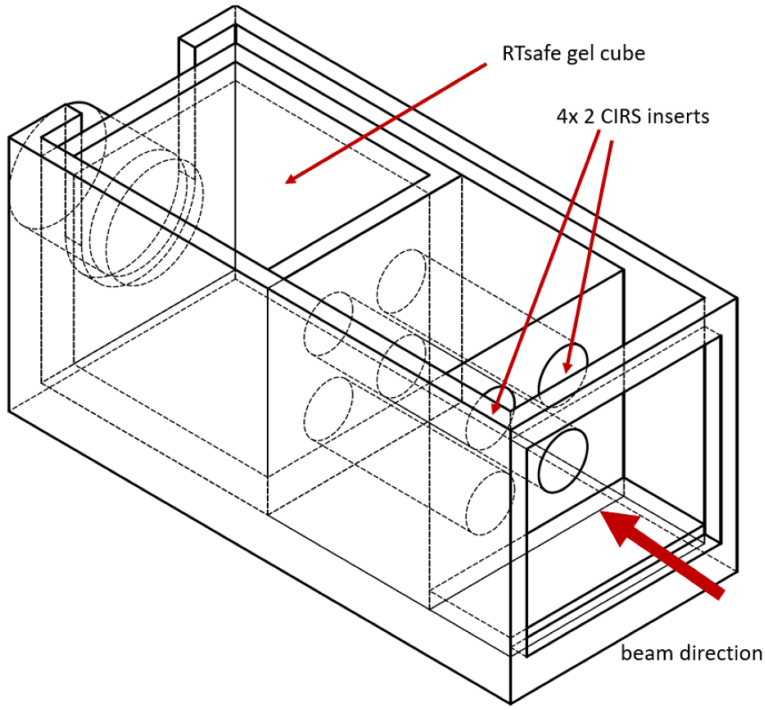

Figure 2. Schematic representation of the assembled phantom equipped with tissue equivalent materials (left) and order of TEM inserts in beam-eye view (a: 2 × Adipose, b: 2 × Muscle, c: 2 × Trabecular Bone, d: 2 × Cortical Bone) and their respective irradiation energy (right). In order to make sure the proton ranges fall within the gel flask, a different proton energy was used for the cortical bone insert.

Table 3. Scan protocols for single and dual-energy scans.

	$SECT_{90}$	$SECT_{120}$	$SECT_{140}$	$DECT_{90}$	$DECT_{150}$
Scanner	Philips Brilliance 16p (single source)			Siemens Somatom Force (dual source)	
Tube potential	90 kVp	120 kVp	140 kVp	90 kVp	150 kVp
$CTDI_{vol}$	20.1 mGy	20.1 mGy	20.1 mGy	30.6 mGy	
Exposure	285 mAs	132 mAs	92 mAs	207 mAs	
Tube current	197 mA	91 mA	64 mA	145 mA	
Voxel size	$0.4 \times 0.4 \times 1.0$ mm^3			$0.4 \times 0.4 \times 1.0$ mm^3	

In addition to the animal tissue samples a third gel flask was combined with a PMMA block with four bores each holding two identical stacked cylindrical CIRS inserts of a different TEM (muscle, adipose, cortical bone and bone 200) (see figure 2).

2.1.2. Imaging calibration phantoms

For calibration of the CT conversion algorithms to the specific x-ray scanners, a cylindrical PMMA phantom was used, containing 12 tissue equivalent cylindrical inserts in sets of four with known composition and density (Gammex RMI, Sun Nuclear Corporation, Melbourne, FL, USA), stacked in the central bore. A similar phantom containing eight different TEMs (CIRS, Computerized Imaging Reference Systems Inc. Norfolk, USA) along a central plane was used to evaluate potential biases of the different SPR conversion methods. All inserts had known RED, atomic composition (from the manufacturer) as well as SPR determined using PKF measurements (see section 2.2).

The calibration phantoms were scanned with the same protocols as the gel phantom (see table 3), and mean Hounsfield units (HU) values for each scan energy and phantom insert within a cylindrical region of interest were calculated and used to fit the various DECT-to-SPR conversion algorithms (see section 2.3) on the specific scan parameters.

2.2. Proton range measurements

2.2.1. PKF

To obtain the ground truth SPR values of both calibration and evaluation phantom inserts, the depth-dose curve of a transmitted proton beam downstream each sample was measured with the PKF. The proton range R^{80}_{insert}, defined as the position of 80% dose in the distal fall-off, was then converted into the corresponding

Table 4. Overview of DECT-to-SPR conversion algorithms and their formalisms for the relative electron density $\hat{\rho}_e$, the effective atomic number Z_{eff}, the ionization potential I, the set of weight fractions of I $\{w_i\}$ and SPR.

		$\hat{\rho}_e$	Z_{eff}	I	$\{w_i\}$	SPR
Segmentation	DECTsp (Landry *et al* 2013a)	Fit $(HU_{\text{L},}, HU_H)$ to $\hat{\rho}_e$ (Saito 2012)	Equation (6), assigned tissue	Equation (5), assigned tissue	Nearest tissue in DECT space	Equation (4)
	EANREDsp (Berndt *et al* 2017)	(Saito 2012)	Fit $HU_{\text{L}}/HU_{\text{L}}$ to Z_{eff} (Landry *et al* 2013b)	Equation (5), assigned tissue	Nearest tissue in EAN RED space	Equation (4)
Decomposition	ETD (Lalonde and Bouchard 2016)	Principal components	Equation (6)	Equation (5)	Principal components	Equation (4)
	BETD (Lalonde *et al* 2017)	Principal components with Bayesian prior	Equation (6)	Equation (5)	Principal components with Bayesian prior	Equation (4)
	Moehler (Wohlfahrt *et al* 2017)	(Saito 2012)	–	–	–	Combine $(HU_{\text{L},}, HU_H)$ and $\hat{\rho}_e$ to input for LUT to SPR/ $\hat{\rho}_e$
Direct Conversion	YLS (Yang *et al* 2010)(Saito 2012)(Landry *et al* 2013b)	(Saito 2012)	(Landry *et al* 2013b)	Fit Z_{eff} to $\ln(I)$ (Yang *et al* 2010)	–	Equation (4)
	(Kanematsu *et al* 2012)	(Saito 2012)	–	–	–	Fit of $\hat{\rho}_e$ to SPR/ $\hat{\rho}_e$
	(Saito 2012, Saito and Sagara 2017)	(Saito 2012)	Fit HU_{L} and $\hat{\rho}_e$ to Z_{eff} (Saito and Sagara 2017)	Fit Z_{eff} to $ln\frac{I}{I_w}$ (Saito and Sagara 2017)	–	Equation (4)

SPRs according to equation (1), with R_x^{80} being the position of 80% of the peak dose in the distal falloff for boxes filled with material x, $l_{\text{insert}} = 50\,\text{mm}$ being the geometrical length of the insert and $\text{SPR}_{\text{air}} = 0.001066$ for 200 MeV protons (Ziegler 1999). Here R_{offset}^{80} refers to the proton range in the water column without any sample in the beam path:

$$\text{SPR}_{\text{insert}} = \frac{R_{\text{offset}}^{80} + l_{\text{insert}} \cdot \text{SPR}_{\text{air}} - R_{\text{insert}}^{80}}{l_{\text{insert}}}. \tag{1}$$

R_{offset}^{80} was measured repeatedly prior to and after measuring the samples, to calculate a standard deviation of the PKF. A set of one-dimensional reference values SPRs for all soft animal tissue samples was measured likewise, both to have an established benchmark for the gel-based measurements and for consistency with previous studies. For this measurement, the sample boxes were placed on a platform (see figure 1 right) and aligned using the laser positioning system to direct the proton beam along the central axis of each box. The sample was then irradiated with a 200 MeV proton pencil beam and the depth-dose profile in the PKF was recorded with 0.1 mm increments. The beam had a full width at half maximum just below 14 mm at isocenter in air, and was therefore sufficiently narrow to traverse the tissue equivalent inserts and tissue samples, with almost negligible range mixing due to tissue heterogeneities. This process was repeated for each box filled with air, purified water and the tissue samples. The SPR was calculated according to equation (2):

$$\text{SPR}_{\text{tissue}} = \frac{R_{\text{tissue}}^{80} - R_{\text{air}}^{80}}{R_{\text{water}}^{80} - R_{\text{air}}^{80}} \cdot (1 - \text{SPR}_{\text{air}}) + \text{SPR}_{\text{air}}. \tag{2}$$

2.2.2. Gel dosimetry

In order to measure proton ranges in three dimensions and with high spatial resolution we used cubic PMMA flasks with 1 cm wall thickness and outer dimensions of 12 × 12 × 14 cm filled with dosimetric N-vinylpyrrolidone based polymer gel (Pappas *et al* 2001) provided by RTsafe (RTsafe P.C., Athens, Greece). Since only a small amount of VIP gel could be produced at a time the cubes had been filled with different batches of gel, which had to be characterized individually. The SPR and WETs of both the cubes and the gel were determined separately with the PKF (see above). To obtain the WET of the gel, we measured each of the three batches separately to confirm consistency. In order to avoid spoiling the dosimetric gel this was done in additional calibration gel flasks with inner dimensions of 5 × 5 × 12 cm using a 200 MeV proton beam in three positions along the short axis of each box. As with the sample boxes this procedure was repeated with empty and water filled calibration boxes.

The soft tissue phantoms were each irradiated with a biological dose of 10 GyE over a 105 × 105 mm^2 185 MeV monoenergetic layer. The TEM phantoms were irradiated with the same total biological dose and a monoenergetic layer of 162 MeV except for a 50 × 50 mm field covering the pair of cortical bone inserts, which was irradiated with 180 MeV instead to ensure that the protons traversing this high SPR material still reach the gel flasks (see figure 2). All fields were irradiated without repainting and with a scan lateral spot separation of 2.5 mm.

Irradiated areas of the gel undergo polymerization that appears as milky coloration (see figure 1, middle). These areas also display a changed spin-spin relaxation rate R_2 that can be detected via MRI, as described by Pappas *et al* (1999), providing a three-dimensional probe of the proton range. The MR images were manually registered to the CT scans using the fiducial on a 1 × 1 × 1 mm^3 grid. A two-dimensional range map was calculated for each gel flask by first subtracting background R_2 values below a threshold and then interpolating the R_2 depth profiles with a 4th order polynomial fit around the dose peak to obtain the 80% distal falloff range RG_{sample}^{80}. Median and standard deviation of the ranges were calculated within a circular ROI with a diameter of 12 mm in the center of each sample, corresponding to the proton beam position in the PKF measurements (FWHM of 14 mm). The SPRs were calculated according to equation (3), using the range in gel RG_{water}^{80} of protons distal to the water reference sample in order to avoid possible systematic errors that could arise. The length $l_{\text{box}} = \left(R_{\text{air}}^{80} - R_{\text{water}}^{80}\right) / (1 - \text{SPR}_{\text{air}})$ refers to the inner dimension of each sample box as measured with the PKF:

$$\text{SPR}_{\text{tissue}} = 1 + \frac{\text{SPR}_{\text{gel}} \times \left(RG_{\text{water}}^{80} - RG_{\text{tissue}}^{80}\right)}{l_{\text{box}}}. \tag{3}$$

MR imaging was performed on a clinical 1.5 T MRI system (Magnetom Aera, Siemens Healthineers, Erlangen, Germany) in a head-coil, using a two-dimensional multi-slice multi-contrast half-Fourier-acquired single-shot turbo spin-echo sequence with a 4200 ms repetition time and echo times of 36 ms, 436 ms, 835 ms and 1230 ms. The resolution was 0.68 mm along the beam axis and in the lateral direction and the slice thickness was 2.5 mm in the vertical direction. This resolution was chosen for practical reasons. However, better resolutions are achievable at the expense of a longer measurement time.

To determine whether the spread in SPR values seen in the converted DECT results for some of the samples results from the CT scanner noise, from inaccuracies in the conversion algorithms or whether it is an accurate representation of actual tissue heterogeneities we investigated the range maps measured with the dosimetric gel, and compared them to the variations obtained with ray tracing on the converted CT images.

2.3. CT scans

All phantoms were scanned with both a DECT scanner (Siemens SOMATOM Definition Force, Siemens Healthineers, Forchheim, Germany) at the Ludwig-Maximilians-University Hospital with tube potentials of 90 kVp and 150 kVp with Sn filtration as well as a SECT scanner with tube potentials of 90 kVp, 120 kVp and 140 kVp (Philips CT Brilliance 16p, Philips Healthcare, Amsterdam, Netherlands) at the Rinecker Proton Therapy Center in Munich, Germany. Table 3 gives an overview of the scan parameters for both CT scanners.

2.4. SPR conversion

All conversion algorithms used in this study were performed voxel-by-voxel on the reconstructed CT images. Table 4 provides an overview of all methods used in this study. The SPR map based on the SECT was obtained using the same HLUT used at a clinical proton facility (XiO treatment planning, Elekta, Stockholm, Sweden) in combination with the 120 kVp CT scan obtained at the clinical SECT scanner.

The DECT-to-SPR conversion algorithms can be divided in three basic approaches that will be briefly explained in the following: segmentation, decomposition and direct conversion. A full description of all methods is given in the supplementary materials. Most DECT-based algorithms aim at generating separate estimates for the RED $\hat{\rho}_e$ and the mean ionization potential I_{tissue} of the scanned tissue. These properties can then be used to calculate the SPR according to

$$\text{SPR} = \hat{\rho}_e \frac{\ln\left(\frac{2m_e c^2 \beta^2}{I(1-\beta^2)}\right) - \beta^2}{\ln\left(\frac{2m_e c^2 \beta^2}{I_w(1-\beta^2)}\right) - \beta^2} \tag{4}$$

where m_e denotes the electron mass, c is the speed of light, $\beta(E)$ the normalized velocity of the protons at a given energy and $I_w = 78\,\text{eV}$ according to ICRU 73 (Ziegler 1999). In this study, we assumed an intermediate proton energy of 100 MeV, corresponding to $\beta = 0.482$.

2.4.1. DECT segmentation

Segmentation-based algorithms aim at assigning a reference tissue out of a selection of published human tissue data to each voxel of the DECT scan. The reference tissue selection is based on tabulated composition and density values tabulated by Woodard and White (1982), White *et al* (1987).

The composition of the assigned reference tissue is used to calculate the mean excitation potential I via the Bragg additivity rule:

$$\ln I = \frac{\sum_i w_i \frac{Z_i}{A_i} \ln I_i}{\sum_i w_i \frac{Z_i}{A_i}} \tag{5}$$

where Z_i denotes the atomic number, A_i the mass number and w_i the proportion of the i th element. These solutions have the additional benefit of providing estimates of other tissue properties such as chemical composition and mass density that would be useful in Monte Carlo based treatment planning (Almeida *et al* 2018) as well as range verification techniques like positron emission tomography (Paganetti and El Fakhri 2015) or prompt-gamma imaging (Hueso-Gonzalez *et al* 2018).

2.4.1.1. DECTspace

One approach based on the work of Berndt *et al* (2017) uses the stoichiometric calibration (Schneider *et al* 1996, Yang *et al* 2010) to predict HU values for human reference tissues and virtual bone tissues for both the high and low energy regime of the DECT scan. Each measured HU value pair of the CT scan is assigned to the reference point with the smallest Euclidian distance in this two-dimensional DECT space.

2.4.1.2. EANREDspace

The second segmentation approach we investigated (Landry *et al* 2013a) starts by assigning effective atomic number Z_{eff} (EAN) and relative electron density $\hat{\rho}_e$ values to each voxel of the DECT image as described in section 2.4.3 and then assigning a reference tissue in the EAN/RED space. In order to account for the covariance between $\hat{\rho}_e$ and Z_{eff} the assignment has to be performed using the Mahalanobis distance rather than the Euclidian distance.

The EAN of the reference tissues is calculated according to Mayneord's equation (6):

$$Z_{\text{eff}} = \left(\frac{\sum_i w_i \frac{Z_i}{A_i} Z_i^m}{\sum_i w_i \frac{Z_i}{A_i}} \right)^{1/m} \tag{6}$$

with w_i being elemental weight fraction of the ith material and $m = 3.3$.

Both segmentation approaches combine the mean excitation energy calculated with the assigned composition according to equation (3) with the RED based on the method by Saito (2012) to obtain the SPR.

2.4.2. DECT decomposition

Decomposition algorithms use known information such as tabulated tissue composition to create a SPR basis and then decompose the scan data in this basis. Like DECT segmentation, these approaches have the advantage of providing a full elemental composition in addition to the SPR.

In this study, we focused on two implementations of the so-called eigentissue decomposition proposed by Lalonde *et al*, one using a simple threshold to assign a different basis based on either soft or bony tissues (ETD) (Lalonde and Bouchard 2016), and the other assigning the bases via Bayesian statistics (BETD) (Lalonde *et al* 2017).

2.4.3. Direct DECT conversion

In the scope of this study, we investigated four published methods to derive a SPR map directly from the DECT image pairs by relying on calibration parameters as well as additional information such as published tissue properties.

Hunemohr *et al* (2014) also used a parametrization for Z_{eff} and $\hat{\rho}_e$, which they combined with the $\ln I$ fit by Yang. Building on this procedure, Mohler *et al* (2016, 2018) suggested to convert the DECT images into a pseudo-monoenergetic image (Wohlfahrt *et al* 2017) (MonoCT). In combination with the $\hat{\rho}_e$-map this MonoCT is converted to a relative cross section image, which can serve as input for a look-up table (LUT) derived from tabulated reference materials to obtain SPR/$\hat{\rho}_e$ (Mohler *et al* 2018).

The YLS algorithm is named after Yang *et al* (2010), and Landry *et al* (2013b), Saito (2012), as it combines procedures proposed by each of these publications. Saito and Landry both propose calibration approaches to convert the DECT images to Z_{eff} and $\hat{\rho}_e$, respectively, whereas Yang parametrizes $\ln I$ as a function of Z_{eff}.

Kanematsu *et al* (2012) proposes a LUT from $\hat{\rho}_e$ to SPR/$\hat{\rho}_e$ based on tabulated tissue data, which we combined with the RED calibration proposed by Saito.

Saito (2012), Saito and Sagara (2017) published a parametrization of $\hat{\rho}_e$ as a function of the weighted sum of the high and low energy DECT image, and Z_{eff} as a function of $\hat{\rho}_e$ and the low energy CT. The logarithm of the mean ionization potential relative to that of water $ln\frac{I}{I_w}$ is then calculated as a function of Z_{eff}. These values are then used as input for equation (4).

3. Results and discussion

3.1. Gel precision and sample homogeneity

In figure 3 (left) the variation (RG^{80}_{insert} − mean $\left(RG^{80}_{\text{insert}}\right)$) of the two-dimensional range-in-gel map within a 20 mm circular region of interest centered around the medial axis of the four TEM insert pairs is shown. The standard deviation across all ROIs was 0.23 mm. This standard deviation is smaller than the resolution of the MR scan in beam direction (0.68 mm), which limits the confidence interval of individual measurements. As the TEM samples were assumed to be homogeneous, this points to a good precision of the gel range measurements. To verify this claim, we integrated the stopping power maps obtained with Saito's DECT conversion along the beam direction and normalized the negative of these maps with the SPR of the dosimetric gel. These 'projected range' variation maps are plotted on the right of figure 3. The standard deviation across all ROIs was 0.18 mm, confirming good homogeneity of the TEM samples.

The same analysis was repeated for the tissue phantoms. The variations of these range-in-gel maps within a 3 cm circular area around the central axis of each sample are depicted in the top of figure 4. The standard deviations of the gel range for the water samples were 0.22 mm (A) and 0.25 mm (E), confirming the precision of the gel ranges in the TEM study. This value can therefore be assumed as a best-case boundary resolution of the mean gel range for this dosimetry setup, encompassing cumulative uncertainties resulting from the MR resolution, possible MR distortions, the image registration, and inhomogeneities of the phantom setup.

The edge at the bottom of sample B could reasonably be explained by imperfections in the dosimetric gel near the walls of the gel flask. The sharper gradients around the center of samples D, F and especially H however point to heterogeneities in the actual tissue samples.

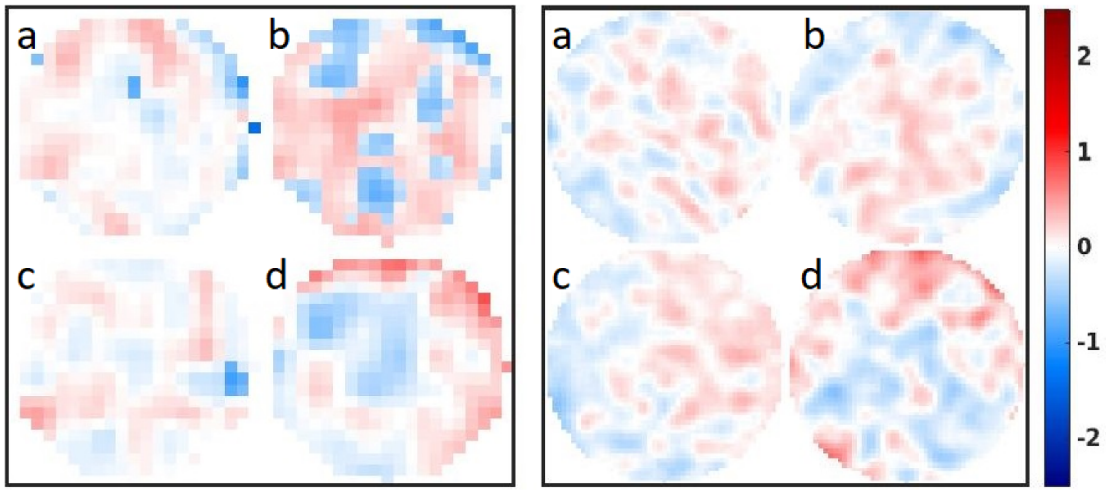

Figure 3. (left) Variation of the detected range in gel ($RG^{80}_{\text{insert}} - mean\left(RG^{80}_{\text{insert}}\right)$) for inserts a–d in within central ROIs with 20 mm diameter (lateral MR resolution 1×1 mm^2). (right) Variation of the projected range in gel based on stopping power maps for inserts a–d in the same ROIs (lateral DECT resolution 0.4×0.4 mm^2). The color scale is in mm.

This was confirmed in the projected range variation maps plotted at the bottom of figure 4. For samples D, F, G and H the variations of the stopping power show similar patterns as the gel ranges, indicating the accuracy of gel dosimetry in detecting tissue variation. The smaller heterogeneities in sample C could not be captured by the gel. This might be a result of proton scattering smearing out the dose profiles recorded by the gel, compared to the ray-tracing integration of SPR values. An in-depth analysis using Monte Carlo simulations could facilitate a more quantitative comparison in the future. Overall, the gel study showed to be a useful tool in analyzing tissue heterogeneities that would be lost in integrated point measurements or low-resolution detectors, indicating that this setup is appropriate for samples that are even more heterogeneous.

The standard deviations σ within the regions of interests mirror this trend, with the largest range variation observed in sample H (1.0 mm), which also shows the largest variation of integrated SPR values (1.7 mm). Table 5 shows an overview of all standard deviations. While no perfectly linear relationship between the two sets of standard deviations could be expected, they do show significant correlation ($p = 0.006$), with a Pearson correlation coefficient of $\rho = 0.86$.

3.2. Gel versus PKF

Table 6 shows a comparison of mean SPR values obtained using the mean ranges in the dosimetric gel relative to the water sample ('gel'), the PKF and by averaging over a cylindrical region of interest of converted CT scans. The single-energy CT ('SECT') result is obtained with the XiO clinical TPS and the dual-energy ('DECT') result on the most accurate DECT-to-SPR conversion based on the method by Saito and Sagara (2017) (see section 3.3).

The SPR values based on the dosimetric gel show good agreement to the benchmark PKF measurements, with mean absolute deviations of only 0.2%. The confidence interval of the gel result was calculated by taking the standard deviation across a circular ROI with a diameter of 12 mm and normal error progression. The resulting average standard deviation of 0.5% was higher than for the PKF, but still sufficiently small for this setup.

In subsequent sections, the SPR values derived from the gel measurements will be considered the ground truth for all tissue phantoms, and the PKF results will be used for the homogeneous plastic phantoms.

3.3. CT-based stopping power conversion

3.3.1. Tissue equivalent materials

Figure 5 shows the spread of SPR values within a region of interest in the converted SPR maps around the ground truth value determined with PKF measurements. The corresponding mean values and standard deviations for one DECT and SECT result are given in table 7. The first eight boxes in each group represent different DECT-to-SPR conversion methods using the dual source dual-energy CT scanner, while the (darkest) box labeled 'SECT' represents the result using the clinical SECT scanner in combination with the XiO TPS. The two segmentation algorithms ('DECTspace' and 'EANREDspace') yielded very similar results for all inserts aside from bone 200, where the latter showed a slightly better agreement with the ground truth.

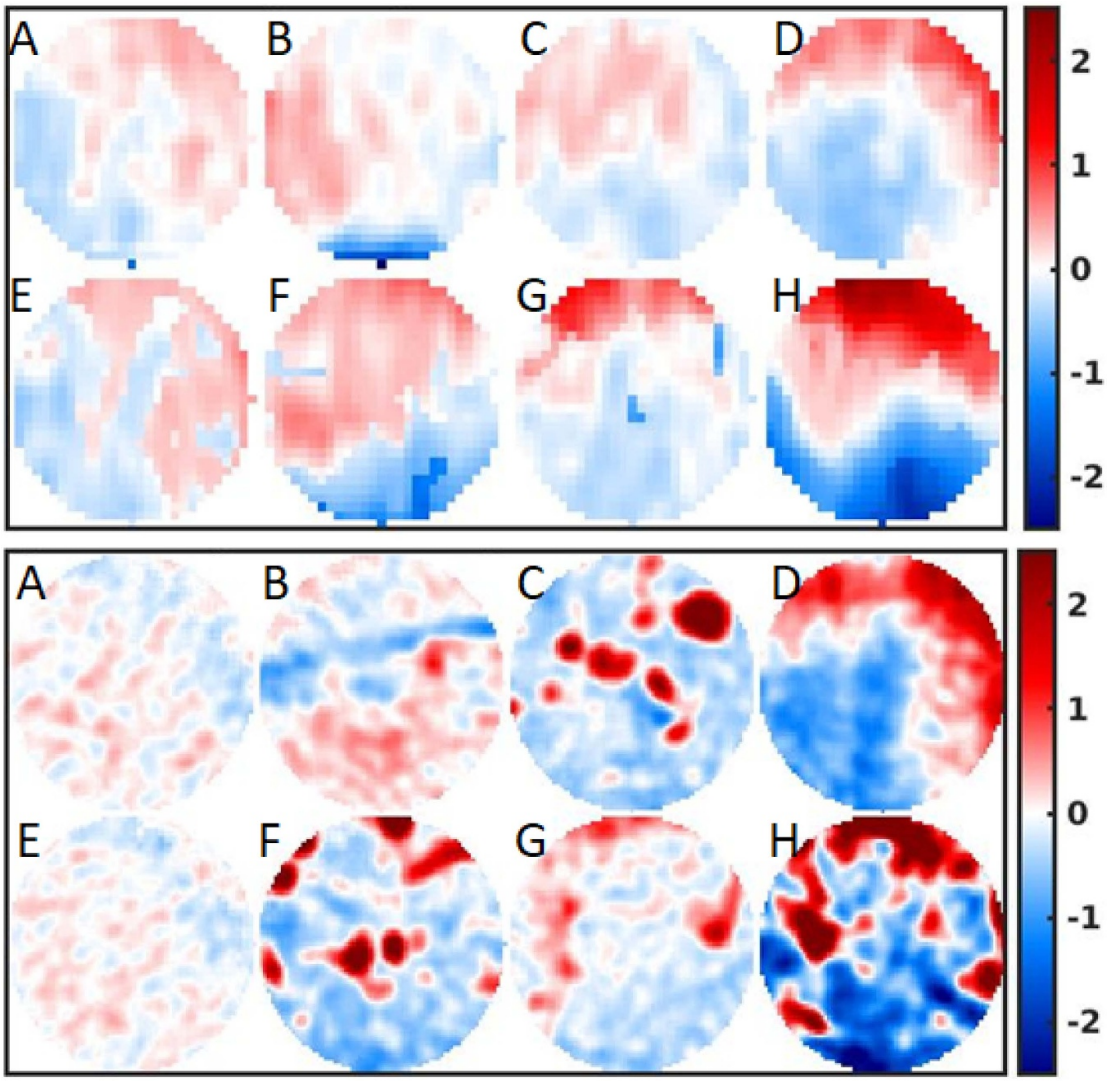

Figure 4. (top) Variation of the *detected* range in gel ($RG^{80}_{\text{insert}} - mean\left(RG^{80}_{\text{insert}}\right)$) for tissue samples A–H in within central ROIs with 30 mm diameter (lateral MR resolution 1×1 mm^2). (bottom) Variation of the *projected* range in gel based on stopping power maps for samples A–H in within the same ROIs (lateral DECT resolution 0.4×0.4 mm^2). The color scale is in mm.

Table 5. Standard deviations σ (in mm) of detected range in gel R80 and integrated SPR values for tissue samples A-H within a central ROI with a 30 mm diameter.

	A	B	C	D	E	F	G	H
σ (range in gel)	0.22	0.35	0.20	0.43	0.25	0.46	0.36	1.02
σ (projected range)	0.16	0.34	0.79	0.86	0.15	0.85	0.37	1.65

The decomposition algorithms ('ETD' and 'BETD') implementations in particular showed divergent results for this insert. This was likely caused by the difference to human tissues of the TEM inserts' composition, in particular the low density of this insert compared to the tabulated bone properties. This sample also resulted in the largest bias for the SECT result. Of the direct conversion approaches, the method by Saito yielded the smallest bias, with median errors of −0.37%. The lowest overall RMSE (1.11%) was achieved with Kanematsu's algorithm. Based on these results none of the dual-energy CT conversion methods showed a clear advantage in terms of agreement with the measured SPRs for TEMs.

3.3.2. Animal tissue samples

The deviation of SPR values of the soft tissue samples to the measured mean SPR are plotted in figure 6. As in the TEM analysis, the SPR values were sampled along a cylindrical region of interest along the length of each sample, corresponding to the area traversed by the proton beam during the PKF probe. In this case the reference is however the gel range.

Table 6. Mean SPR (with standard deviations in brackets) based on the gel dosimetry, PKF measurements and converted single- and dual-energy CTs. The deviations in percent are in comparison to the reference values obtained with the dosimetric gel scan (first column).

	SPR (gel)	SPR (PKF)	Deviation /%	SPR (SECT)	Deviation /%	SPR (DECT)	Deviation /%
B	1.054(1)	1.055(1)	0.09	1.04(1)	−1.3	1.05(2)	−0.38
C	1.035(1)	1.032(1)	−0.29	1.03(4)	−0.48	1.03(4)	−0.48
D	1.025(2)	1.022(1)	−0.29	1.02(1)	−0.49	1.03(2)	0.49
F	1.069(2)	1.069(1)	0.00	1.05(6)	−1.77	1.07(5)	0.09
G	1.061(2)	1.062(1)	0.09	1.049(5)	−1.13	1.06(1)	−0.08
H	0.952(5)	0.947(1)	0.53	0.95(4)	−0.21	0.96(4)	0.84

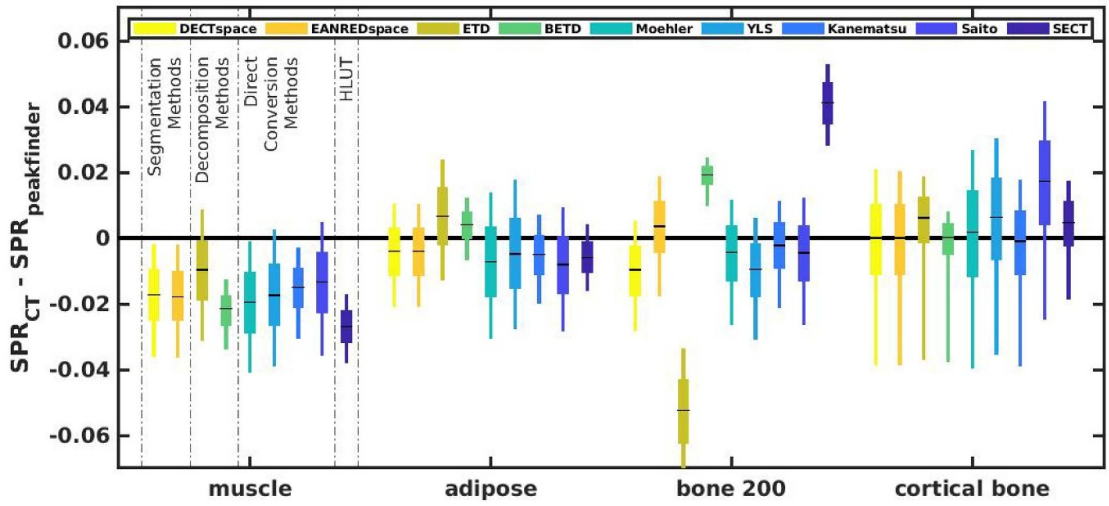

Figure 5. Deviation of CT-based SPR values within a cylindrical region of interest in the TEM inserts from the ground truth obtained with the PKF. The central line in each box marks the median, the boxes extend between the 15.9th and 84.1th percentiles and the whiskers cover all data points within an interquartile range from the 2.5th and 97.5th percentiles, corresponding to one and two standard deviations, respectively.

Table 7. Mean SPR (with standard deviations in brackets) based on the PKF measurements as well as single- and dual-energy CTs, converted with the XiO TPS and Saito's method. The deviations in percent are in comparison to the reference values obtained with the PKF scan.

	SPR (PKF)	SPR (SECT)	Deviation /%	SPR (DECT)	Deviation /%
Muscle	1.059(1)	1.032(6)	−2.51	1.05(1)	−1.21
Adipose	0.975(1)	0.969(5)	−0.58	0.97(1)	−0.81
Bone200	1.116(1)	1.157(7)	3.72	1.11(1)	−0.37
Cortical bone	1.688(1)	1.69(2)	−0.29	1.7057(2)	1.05

The standard deviation of the DECT-based values was again higher than for the SECT-based result, and this trend was more pronounced than for the homogeneous TEM inserts. The overall variation was also higher across all DECT methods, especially in samples D (beef tongue) and H (beef fat). The latter in particular exhibited large negative deviation to the median gel result, likely due to the unavoidable presence of air bubbles in this sample. Since the analyzed tissues were not fully homogeneous, as seen in the range-in-gel maps (see figure 4), this could indicate an accurately detected variation in the tissues.

The two segmentation methods (DECTspace and EANREDspace) again performed very similarly in terms of precision and accuracy, with mean absolute differences of 0.4% (compared to −1.2% for SECT). The BETD had the second lowest bias (−0.2) as well as by far the lowest standard variation (1.5% compared to 2.9% for SECT) among all methods. The ETD without Bayesian analysis performed significantly worse in realistic noise conditions, mirroring the simulation study of Hudobivnik *et al* (2016). The direct conversion algorithms (Moehler, YLS, Kanematsu and Saito) all yielded similarly good results.

Overall, the DECT conversion algorithms yielded more accurate results in animal tissues than in TEM. This was expected, since the composition of these samples more closely resembled the tabulated human tissue compositions used to calibrate the CT conversion methods than the tissue equivalent plastic materials.

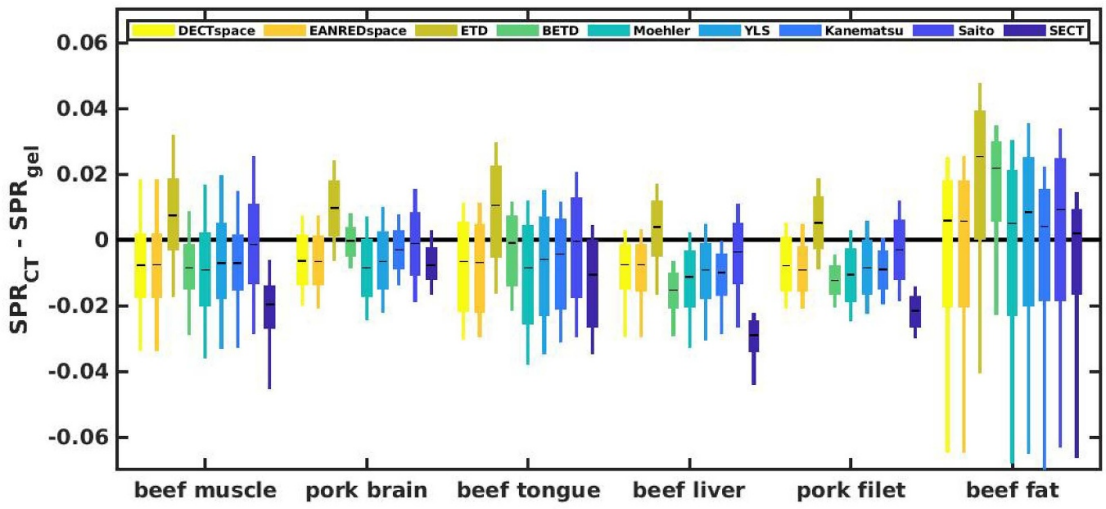

Figure 6. Deviation of dual source DECT and SECT-based SPR values within a cylindrical region of interest from the reference values obtained with gel dosimetry. The central line in each box marks the median, the boxes extend between the 15.9th and 84.1th percentiles and the whiskers cover all data points within an interquartile range from the 2.5th and 97.5th percentiles, corresponding to one and two standard deviations, respectively.

Table 8. Median relative difference (MRD) to gel reference and standard deviation (std) for SPR values based on the dual source DECT scanner (DSS) and clinical sequential DECT (SEQ). All numerical values are in percent.

		DECTsp	EANREDsp	ETD	BETD	Moehler	YLS	Kanematsu	Saito	SECT
DSS	MRD	−0.5	−0.5	1.0	−0.2	−0.7	−0.4	−0.5	0.01	–
	std	2.7	2.7	2.6	1.5	2.8	2.8	2.7	2.8	
SEQ	MRD	−0.2	−1.1	−1.4	3.1	−1.1	0.1	−0.9	−0.4	−1.4
	std	3.8	3.8	5.4	1.8	4.2	4.2	3.7	4.1	2.9

Based on these results, no DECT conversion method had a major advantage over all others, but all the investigated algorithms yielded an improved accuracy compared to the clinical SECT conversion. The method by Saito and Sagara (2017) yielded the most accurate results, with mean absolute differences of only 0.25% and the smallest median bias of only 0.01%. Table 8 shows an overview of the median difference and standard deviations for all conversion methods.

A two-sided Wilcoxon signed rank test was applied, which showed that all results except for the ETD without Bayesian analysis and the single-energy HLUT were in agreement with the measured values at a 5% significance level.

3.4. Scanner comparison

The DECT scans were obtained once with a dedicated dual source dual-energy scanner and once by running two sequential CT scans with different energies on a clinical SECT scanner. Figure 7 shows an overview of the stopping power values obtained with two sequential SECT scans for both the TEMs (top) and fresh tissue samples (bottom). The sequential DECT images showed a higher noise level than the images obtained with the dedicated DECT scanner (see figures 5 and 6). This resulted in a larger spread of SPR values across all samples and conversion methods, which particularly affected the YLS result of the cortical bone TEM sample and the ETD method. Apart from these exceptions, the accuracy of the median SPR values of the tissue substitutes showed an accuracy comparable to the previous results based on the dual source scanner.

For the tissue samples, the higher image noise resulted in an increase of 15% to 53% in the standard deviations for the different methods (see table 8). The BETD resulted in the by far smallest variation, but at the expense of also having the lowest accuracy with a bias of +3.1%. The DECTspace segmentation and the YLS performed best on the sequential scan data, closely followed by the results based on Saito's method.

A two-sided Wilcoxon test showed statistically significant differences to the measured values within a 5% significance level for all results except of the DECT segmentation, ETD and the YLS and Saito approach. This decrease in accuracy was expected, given the smaller energy separation (90kVp to 140kVp compared to 90kVp to 150kVp with Sn filtration for the dual source DECT scanner) and the higher noise due to the lower dose limit and different reconstruction algorithm. Still, the majority of DECT conversion methods could improve the accuracy of the SPR prediction relative to the clinical SECT conversion.

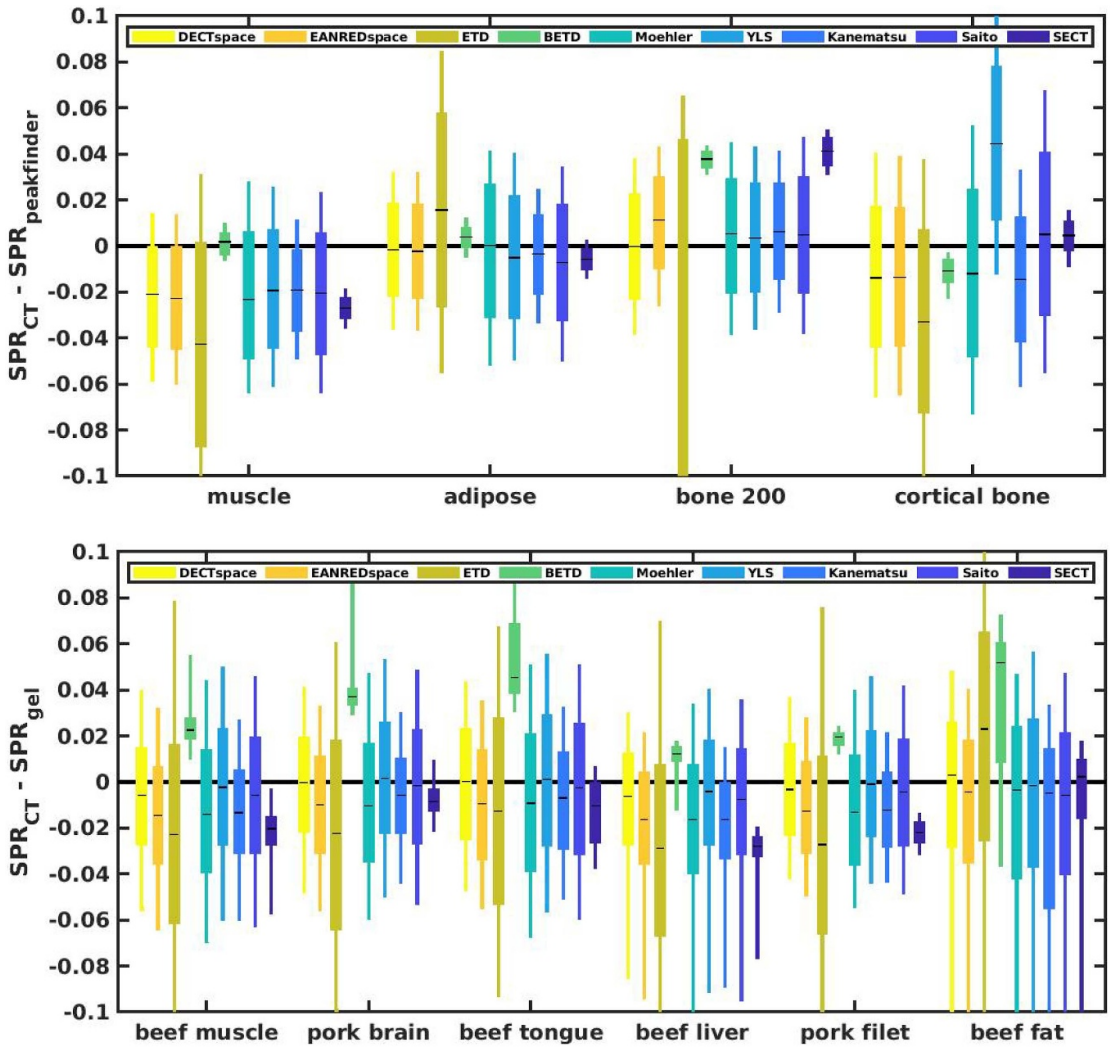

Figure 7. Deviation of sequential DECT and SECT-based SPR values within a cylindrical region of interest from the reference values obtained with the PKF (top) and gel (bottom). The central line in each box marks the median, the boxes extend between the 15.9th and 84.1th percentiles and the whiskers cover all data points within an interquartile range from the 2.5th and 97.5th percentiles, corresponding to one and two standard deviations, respectively.

4. Conclusion

In this study, eight DECT formalisms for SPR conversion and one clinical SECT formalism were for the first time validated in TEMs and animal tissue samples with a high-resolution three-dimensional detector. This setup was benchmarked against a variable water column reference showing great accuracy of the median SPR values and a superior performance in capturing inhomogeneities of the tissue samples. The various published methods were analyzed under the same conditions, yielding similar accuracy for all DECT conversion methods, except for a small advantage for the method by Saito *et al*. Additionally, the DECT conversions were applied to a sequential DECT scan on a conventional SECT scanner which also resulted in improvements over the single-energy result, but a slightly lower accuracy of the mean value and a significantly increased variation compared to the dual source DECT.

Acknowledgments

This work was funded by the German Research Foundation (DFG) research training group GRK 2274, and the Munich Center for Advanced Photonics (MAP). The authors would like to thank Daniel Köpl and the team of Rinecker Proton Therapy Center for their support during the proton irradiation and subsequent scans as well as Dr Bastian Sabel and Dr Christopher Kurz for their assistance for the DECT scanning at Ludwig-Maximilian University Hospital. Also, they are grateful to Dr Patrick Wohlfahrt and Dr Christian Richter from Oncoray Dresden, as well as Dr Christian Mohler and Dr Steffen Greilich from the German

Cancer Research Center Heidelberg for fruitful discussions on their DECT to SPR conversion method investigated in this study. Finally, they acknowledge Professor Dr Frank Verhaegen and Dr Isabel de Almeida for several stimulating discussions and collaborative efforts on DECT.

ORCID iDs

M Wuerl https://orcid.org/0000-0003-3044-449X
M Pinto https://orcid.org/0000-0001-6835-2561
O Dietrich https://orcid.org/0000-0001-6182-5039
A Lalonde https://orcid.org/0000-0002-8715-8235

References

Almeida I P *et al* 2018 Monte Carlo proton dose calculations using a radiotherapy specific dual-energy CT scanner for tissue segmentation and range assessment *Phys. Med. Biol.* **63** 115008
Bär E *et al* 2017 Experimental validation of two dual-energy CT methods for proton therapy using heterogeneous tissue samples *Med. Phys.* **45** 48–59
Berndt B *et al* 2016 TH-CD-202-05: DECT based tissue segmentation as input to Monte Carlo simulations for proton treatment verification using PET imaging *Med. Phys.* **43** 3877–8
Berndt B *et al* 2017 Application of single- and dual-energy CT brain tissue segmentation to PET monitoring of proton therapy *Phys. Med. Biol.* **62** 2427–48
Bourque A E, Carrier J F and Bouchard H 2014 A stoichiometric calibration method for dual energy computed tomography *Phys. Med. Biol.* **59** 2059–88
Cormack A M 1963 Representation of a function by its line integrals with some radiological applications *J. Phys. D: Appl. Phys.* **34** 2722-&
Dedes G *et al* 2019 Experimental comparison of proton CT and dual energy x-ray CT for relative stopping power estimation in proton therapy *Phys. Med. Biol.* **64** 165002
Hillbrand M *et al* 2019 Gel dosimetry for three dimensional proton range measurements in anthropomorphic geometries *Z. Med. Phys.* **29** 162–72
Hudobivnik N *et al* 2016 Comparison of proton therapy treatment planning for head tumors with a pencil beam algorithm on dual and single energy CT images *Med. Phys.* **43** 495
Hueso-Gonzalez F, Rabe M, Ruggieri T A, Bortfeld T and Verburg J M 2018 A full-scale clinical prototype for proton range verification using prompt gamma-ray spectroscopy *Phys. Med. Biol.* **63** 185019
Hunemohr N, Krauss B, Dinkel J, Gillmann C, Ackermann B, Jäkel O and Greilich S 2013 Ion range estimation by using dual energy computed tomography *Z. Med. Phys.* **23** 300–13
Hunemohr N, Krauss B, Tremmel C, Ackermann B, Jäkel O and Greilich S 2014 Experimental verification of ion stopping power prediction from dual energy CT data in tissue surrogates *Phys. Med. Biol.* **59** 83–96
Kanematsu N, Inaniwa T and Koba Y 2012 Relationship between electron density and effective densities of body tissues for stopping, scattering, and nuclear interactions of proton and ion beams *Med. Phys.* **39** 1016–20
Lalonde A, Bär E and Bouchard H 2017 A Bayesian approach to solve proton stopping powers from noisy multi-energy CT data *Med. Phys.* **44** 5293–302
Lalonde A and Bouchard H 2016 A general method to derive tissue parameters for Monte Carlo dose calculation with multi-energy CT *Phys. Med. Biol.* **61** 8044–69
Lalonde A, Simard M, Remy C, Bär E and Bouchard H 2018 The impact of dual- and multi-energy CT on proton pencil beam range uncertainties: a Monte Carlo study *Phys. Med. Biol.* **63** 195012
Landry G, Parodi K, Wildberger J E and Verhaegen F 2013a Deriving concentrations of oxygen and carbon in human tissues using single- and dual-energy CT for ion therapy applications *Phys. Med. Biol.* **58** 5029–48
Landry G, Reniers B, Granton P V, van Rooijen B, Beaulieu L, Wildberger J E and Verhaegen F 2011 Extracting atomic numbers and electron densities from a dual source dual energy CT scanner: experiments and a simulation model *Radiother. Oncol.* **100** 375–9
Landry G, Seco J, Gaudreault M and Verhaegen F 2013b Deriving effective atomic numbers from DECT based on a parameterization of the ratio of high and low linear attenuation coefficients *Phys. Med. Biol.* **58** 6851–66
Mohler C, Russ T, Wohlfahrt P, Elter A, Runz A, Richter C and Greilich S 2018 Experimental verification of stopping-power prediction from single- and dual-energy computed tomography in biological tissues *Phys. Med. Biol.* **63** 025001
Mohler C, Wohlfahrt P, Richter C and Greilich S 2016 Range prediction for tissue mixtures based on dual-energy CT *Phys. Med. Biol.* **61** N268–75
Paganetti H 2012 Range uncertainties in proton therapy and the role of Monte Carlo simulations *Phys. Med. Biol.* **57** R99–117
Paganetti H and El Fakhri G 2015 Monitoring proton therapy with PET *Br. J. Radiol.* **88** 20150173
Pappas E, Maris T, Angelopoulos A, Paparigopoulou M, Sakelliou L, Sandilos P, Voyiatzi S and Vlachos L 1999 A new polymer gel for magnetic resonance imaging (MRI) radiation dosimetry *Phys. Med. Biol.* **44** 2677–84
Pappas E, Seimenis I, Angelopoulos A, Georgolopoulou P, Kamariotaki-Paparigopoulou M, Maris T, Sakelliou L, Sandilos P and Vlachos L 2001 Narrow stereotactic beam profile measurements using N-vinylpyrrolidone based polymer gels and magnetic resonance imaging *Phys. Med. Biol.* **46** 783–97
Penfold S N, Rosenfeld A B, Schulte R W and Schubert K E 2009 A more accurate reconstruction system matrix for quantitative proton computed tomography *Med. Phys.* **36** 4511–8
Rit S *et al* 2013 Filtered backprojection proton CT reconstruction along most likely paths *Med. Phys.* **40** 031103
Saito M 2012 Potential of dual-energy subtraction for converting CT numbers to electron density based on a single linear relationship *Med. Phys.* **39** 2021–30
Saito M and Sagara S 2017 Simplified derivation of stopping power ratio in the human body from dual-energy CT data *Med. Phys.* **44** 4179–87

Schneider U, Pedroni E and Lomax A 1996 The calibration of CT Hounsfield units for radiotherapy treatment planning *Phys. Med. Biol.* **41** 111–24

Taasti V T, Michalak G J, Hansen D C, Deisher A J, Kruse J J, Krauss B, Muren L P, Petersen J B B and Mccollough C H 2017 Validation of proton stopping power ratio estimation based on dual energy CT using fresh tissue samples *Phys. Med. Biol.* **63** 015012

Taasti V T, Petersen J B B, Muren L P, Thygesen J and Hansen D C 2016 A robust empirical parametrization of proton stopping power using dual energy CT *Med. Phys.* **43** 5547

Takada Y, Kondo K, Marume T, Nagayoshi K, Okada I and Takikawa K 1988 Proton computed-tomography with a 250 Mev pulsed-beam *Nucl. Instrum. Methods Phys. Res.* A **273** 410–22

White D R, Woodard H Q and Hammond S M 1987 Average soft-tissue and bone models for use in radiation dosimetry *Br. J. Radiol.* **60** 907–13

Wohlfahrt P *et al* 2017 Evaluation of stopping-power prediction by dual- and single-energy computed tomography in an anthropomorphic ground-truth phantom *Int. J. Radiat. Oncol. Biol. Phys.***100** 244–253

Wohlfahrt P, Möhler C, Hietschold V, Menkel S, Greilich S, Krause M, Baumann M, Enghardt W and Richter C 2017 Clinical implementation of dual-energy CT for proton treatment planning on pseudo-monoenergetic CT scans *Int. J. Radiat. Oncol. Biol. Phys.* **97** 427–34

Wohlfahrt P, Möhler C, Stützer K, Greilich S and Richter C 2017 Dual-energy CT based proton range prediction in head and pelvic tumor patients *Radiother. Oncol.* **125** 526–33

Woodard H Q and White D R 1982 Bone models for use in radiotherapy dosimetry *Br. J. Radiol.* **55** 277–82

Xie Y, Ainsley C, Yin L, Zou W, Mcdonough J, Solberg T D, Lin A and Teo B-K K 2018 *Ex vivo* validation of a stoichiometric dual energy CT proton stopping power ratio calibration *Phys. Med. Biol.* **63** 055016

Yang M, Virshup G, Clayton J, Zhu X R, Mohan R and Dong L 2010 Theoretical variance analysis of single- and dual-energy computed tomography methods for calculating proton stopping power ratios of biological tissues *Phys. Med. Biol.* **55** 1343–62

Zhu J and Penfold S N 2016 Dosimetric comparison of stopping power calibration with dual-energy CT and single-energy CT in proton therapy treatment planning *Med. Phys.* **43** 2845–54

Ziegler J F 1999 Comments on ICRU report no. 49: stopping powers and ranges for protons and alpha particles *Radiat. Res.* **152** 219–22